MECHANISMS OF SINGLE-WALL CARBON NANOTUBE GROWTH BY THE LASER VAPORIZATION TECHNIQUE: IN SITU IMAGING AND SPECTROSCOPY

D. B. GEOHEGAN[*], A. A. PURETZKY[**], X. FAN[*], M. A. GUILLORN[*], M. L. SIMPSON[*], V. I. MERKULOV[*], S. J. PENNYCOOK[*]
[*]Oak Ridge National Laboratory, Oak Ridge, TN 37831, odg@ornl.gov
[**]Dept. of Materials Science and Engineering, University of Tennessee

ABSTRACT

Single-wall carbon nanotubes are formed by Nd:YAG laser vaporization of a graphite/(1 at. % Ni, 1 at. % Co) target into flowing argon (500 Torr) within a quartz tube furnace (1000 ^{o}C). Here, this process is investigated for the first time with time-resolved laser-induced luminescence imaging and spectroscopy of Co atoms, C_2 and C_3 molecules, and clusters. These measurements under actual synthesis conditions show that the plume of vaporized material is segregated and confined within a vortex ring which maintains a ~1 cm^3 volume for several seconds. Using time-resolved spectroscopy and spectroscopic imaging, the time for conversion of atomic and molecular species to clusters was measured for both carbon (200 μs) and cobalt (2 ms). This rapid conversion of carbon to nanoparticles, combined with transmission electron microscopy analysis of the collected deposits, indicate that nanotube growth occurs during several seconds of time from a feedstock of mixed nanoparticles in the gas-suspended plume. Using these in situ diagnostics to adjust the time spent by the plume within the high-temperature zone, single-walled nanotubes of controlled length were grown at an estimated rate of 0.2 μm/s .

INTRODUCTION

In addition to the growth of thin films by pulsed laser deposition, laser vaporization is an established nanomaterial synthesis tool. It is arguably the best method to grow high-quality, high-purity single-wall carbon nanotubes (SWNTs). As typically employed, a small amount of material (~ 10^{16} carbon atoms and ~10^{14} metal catalyst atoms, e.g. ~ 1 at. % Ni, Co, Fe, Y, etc.) is laser-vaporized inside a hot oven with gently-flowing inert gas[1]. On a single laser shot [2], this material self-assembles to form an astounding fraction of SWNT (70-90 vol.% yield) under the correct conditions [1,3]. This same technique can be applied to form solid nanorods and nanowires of many other materials [4].

The conditions for SWNT growth are very similar to those for carbon fullerene production, except for the presence of metal catalyst nanoparticles which form during the process and catalyze the growth of the carbon nanotubes. Despite the wide range of metal catalyst nanoparticle diameters produced during pulsed-LV, under the appropriate conditions larger multiwalled nanotubes can be suppressed and exclusively SWNT can be formed. While SWNT grow easily by nanosecond time-scale laser vaporization followed by annealing in a hot oven, they can also be grown by LV at room temperature where it appears that sufficient heating of the target or ejecta is accomplished by high repetition rate [5] or long-pulse (~ 10 ms) [6] lasers.

SWNTs exhibit remarkable electronic and structural properties which promise to revolutionize application areas from nanoscale electronics to ultralightweight structural materials [7]. In the six years since SWNTs were discovered [8,9], research on their electronic properties and chemical functionalization has provided strong evidence that carbon nanotubes (in striking contrast to earlier fullerenes) will enable major advances in nanoscale electronic devices [10], Micro Electro Mechanical Systems (MEMS) [11, 12], biological probes [13], and field emission devices [14, 15]. Possibly of greatest significance, nanotubes may serve as molecular wires for input/output paths and interconnects between molecular electronic components or devices. Recent experiments also show that SWNT are highly thermally conductive [7], resistant to high temperatures and harsh chemicals [16], lightweight [17], incredibly strong in the axial direction (1–TPa Young's modulus) and resilient in the transverse [12], and their hollow structure makes them ideal for hydrogen storage [17] and drug delivery. These properties broaden the scope of nanotube applications into aerospace, transportation, and biotechnology.

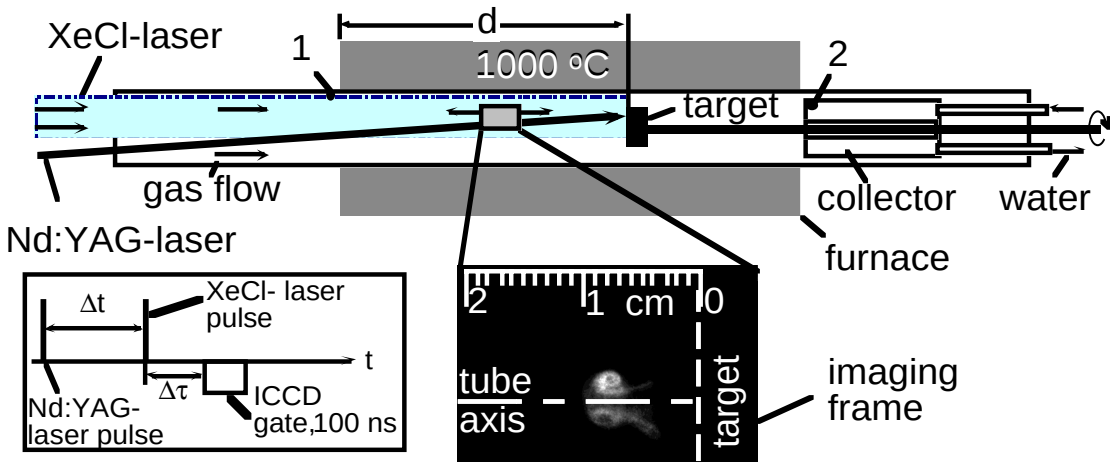

Fig. 1. Schematic of the 2"-diameter quartz-tube and hot furnace used for laser vaporization growth of SWNT with in situ Laser-Induced Luminescence (LIL) -imaging and spectroscopy diagnostics. Beam geometries and imageable area are indicated. The black dots and the numbers show the collection points of the ablated material: 1-upstream; 2-collector. The C/Ni/Co target was positioned at two distances, d, from the front of the furnace. The inset on the left shows the relative timing between ablation (Nd:YAG) and and LIL-probe (XeCl) laser pulses (Δt), and the ICCD gate delay after the XeCl laser, ($\Delta\tau$). The ICCD camera system recorded the LIL from the plume after a carbon target (containing 1 at. % Ni, and 1 at. % Co) was laser-vaporized in 500 Torr Ar at 1000° C. Optical emission spectra were recorded at each image position with a spectrometer and gated, intensified diode array.

Up until now, three principal methods have been used to synthesize carbon nanotubes. These include laser vaporization (LV) [18], dc-arc vaporization (AV) [8, 9, 19], and chemical vapor deposition (CVD) [20, 21]. Unlike CVD, both LV and AV now produce nearly exclusively SWNT. However, very little is known about where and when the SWNT are formed in LV or AV growth chambers, the identity of the precursor species, and the growth rates.

The development of methods for large-scale production of SWNT (for structural and other applications) await measurements to determine their growth rate using current synthesis techniques, and methods to increase it toward the theoretical maximum. However nanotube growth is not controlled or understood. In situ diagnostics have not been applied during growth, and therefore no mechanisms have been determined to control the atomic-scale structure (chirality) of nanotubes during synthesis. Since the electronic properties of chemically-unmodified SWNTs are entirely determined by their chirality, electronic transport in as-grown nanotubes is currently uncontrolled.

Pulsed-LV with nanosecond lasers is especially amenable to diagnostic investigations. The vaporizing pulse lasts only ~10 ns and SWNT growth then can occur undisturbed from further excitation, even for single laser ablation events [2]. Recent spectroscopic measurements of the luminous laser plasma have been made for pulsed-LV at early times after Nd:YAG laser ablation (< 200 μs) [22] and after long-pulse CO_2 laser ablation at room temperature [6]. However, these measurements were limited to times while the ablated material is still quite hot.

Recently laser induced luminescence (LIL), gated intensified charge-coupled device (ICCD) imaging, and optical emission spectroscopy were applied to understand how nanoparticles form and grow in pulsed laser ablation plumes at room temperature [23-25]. In this study these techniques are applied to understand how SWNT grow from laser-vaporized carbon and catalyst species under typical growth conditions at high temperatures.

EXPERIMENTAL

The SWNT growth setup in Fig. 1 was fashioned after that used by Guo et al. [18]. It consists of a quartz tube (2 in. diameter, 24 in. length) mounted inside a hinged tube furnace (12 in. length) operating at 1000°C. The quartz tube was O-ring sealed to standard 4.5-in.-Conflat vacuum components. The ablation and probe laser beams entered through the same Suprasil window which was mounted in a vacuum flange. Argon gas was introduced around this window, controlled at 100 sccm to maintain a 500 Torr pressure, and pumped out through a needle valve downstream of a brass, water-cooled collector which was inserted into the quartz tube and positioned just outside the oven.

A 1-in. diameter graphite target containing 1 at. % each of Ni (Alfa, 2.2-3.0 μm, 99.9%) and Co (Alfa, 1-6 μm, 99.8%) powders was prepared with the carbon cement (Dylon GC) procedure described in Ref. 2. The target was screwed onto a 0.25-in. diameter graphite rod and was rotated during operation. This rod was mounted along the tube axis through a hole in the collector. The ablation laser (Nd:YAG, 8-ns FWHM pulse) beam was focused to a 1.6 mm-diameter, donut-shaped spot on the target. Both the 1.06-μm fundamental and the 532-nm 2nd-harmonic were used (with no time delay) to provide a total energy of 140 mJ at the target. An unfocused, time-delayed XeCl-laser pulse (308 nm, 30-ns FWHM, 20 mJ/cm^2) was used to induce luminescence in the ablation plume.

To permit imaging of the plume with a gated ICCD-camera system (Princeton Instruments, 5-ns minimum gate, 200–820 nm spectral range) the furnace was opened for ~ 3 seconds/per image. Alternatively, at each plume location lenses collected the plasma emission and/or laser-induced luminescence for optical emission spectroscopy using a 0.3-m spectrometer (Acton VM-503, resolution either 10 nm or 1.3 nm) with an intensified, gated diode array (Princeton Instruments IRY-700RB).

Carbon nanotubes were synthesized under a variety of laser repetition rates, flow conditions, target positions, and numbers of total shots on the target. Following each run, deposits were collected at various points in the reactor and analyzed by bright-field TEM for correlation with the transport dynamics observed during the run with time-resolved imaging and/or spectroscopy.

When the target was positioned d = 21 cm from the front of the furnace, ~ 10 μm-long SWNT bundles comprised very high fractions of the deposit found downstream on the collector. Figure 2(a) shows a field-emission SEM image of a deposit produced at a laser repetition rate of only 0.016 Hz. From 70–90% of the deposit appears to consist of SWNT bundles as estimated from an areal analysis. Bright-field TEM images as in Fig. 2(b) show that metal catalyst nanoparticles (mixed Ni/Co composition, ~ 1:1 stoichiometry) and small amounts of amorphous carbon account for the rest of the deposit (as described in the literature) [1, 3, 18]. High-resolution scanning TEM images such as those in Fig. 3(a) confirm that the bundles consist of

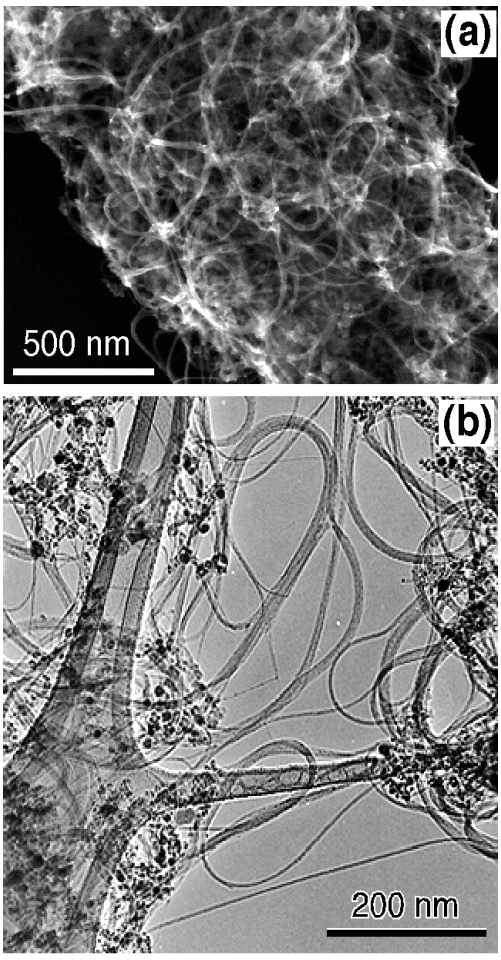

Fig. 2. (a) Field-emission SEM image of SWNT bundles, metal catalyst particles, and unconverted carbon soot produced by laser ablation of a C/Ni/Co target at 1000 ^{o}C. **(b)** TEM images of the raw soot collected: downstream on the collector (point 2, for d=21 cm in Fig.1), showing a very high fraction of SWNT bundles along with metal nanoparticles (black dots).

SWNT. Cross-sectional images of the bundles permit an estimate of the nanotube diameters, as shown in Fig. 3b.

The ability to correlate these TEM and FESEM images of deposits with the plume transport dynamics (observed with in situ diagnostics, described below) permits conclusive assessment of the growth conditions. For example, the long nanotubes collected in Fig. 2 were created on single laser shots. In situ imaging proved that each plume completely cleared the growth chamber before the next laser shot.

To understand where and when nanotubes grow, ICCD imaging and spectroscopy of the C/Ni/Co plume were performed at different times after laser vaporization, Δt, spanning 20 ns $\leq \Delta t \leq$ 3s. A detailed comparison between the plume dynamics at room temperature and at 1000°C is given in Refs. 26 and 27.

At early times ($\Delta t \leq 200$ μs) after the Nd: YAG laser vaporizing pulse, the ablated material is primarily in excited states and can be imaged directly from its plasma emission alone (without LIL-excitation). A comparison of the Nd:YAG-laser-generated plume propagation at room temperature and at 1000 °C for $\Delta t \leq 200$ μs is presented in detail in Ref. 27. In each case, the plume exhibits oscillations in both axial and radial directions. These oscillations are evident from a plot of the leading edge position of the plume vs. time given in Fig. 6. The reason for these oscillations involves the interaction of the bubble of plume material with the high-pressure (500 Torr) background gas. Just after ablation, the plume expands both radially and axially and compresses the background gas. However, the initial kinetic energy of the plume contributes to its overexpansion into the background gas, and it expands past the position where the plume pressure is equals that of the surrounding ambient. Recovering from this overexpansion, a backward motion is induced in the plume. In addition, a backward motion in the radial direction results in an axial focusing of the plume.

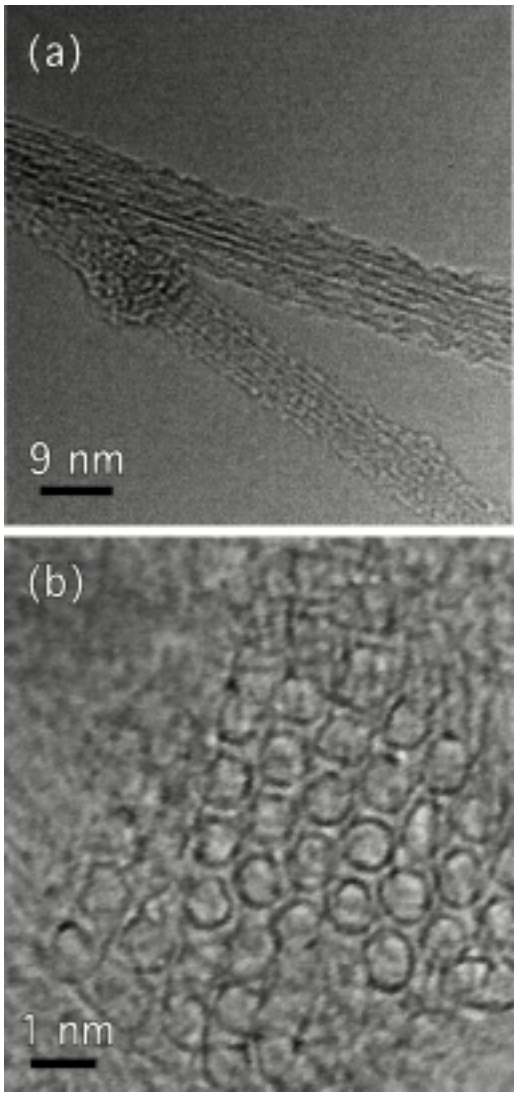

Fig. 3. (a) HRTEM images of bundles of SWNTs grown by laser ablation at 1000 °C. **(b)** A cross-section of a nanotube bundle, revealing the shape and diameters of

At 1000°C, four axial oscillations, decaying in strength, are evident in Figure 6 (at 40 ns, 200 ns, 2μs, and 200 μs). At room temperature, three oscillations can be seen at 600 ns, 10 μs, and 300 μs. These oscillations result from the propagation of internal shock waves within the plume material, caused when the strong external shock wave is generated and detaches to propagate through the background gas. The plume material reflected from the contact surface between the plume and the background gas forms the internal shocks within the plume. These internal shocks serve to mix and additionally heat the atomic and molecular carbon and the catalyst species within the plume. This oscillatory behavior of laser plasmas propagating into background gases has been observed before[28-31] and has been described theoretically [30].

Following these plume oscillations [28, 29] during $\Delta t \leq 0.2$ ms, the ablated material is segregated into a vortex ring [30, 31] (or "smoke ring") [23] shown at $\Delta t = 0.2$ ms in Figs. 5(a),(b). This vortex ring is generated because of the viscous interaction between the plume and the background gas. Vortex formation efficiently mixes the ablated species with the background gas, promoting clustering of the plume species through three-body collisions. Then the vortex

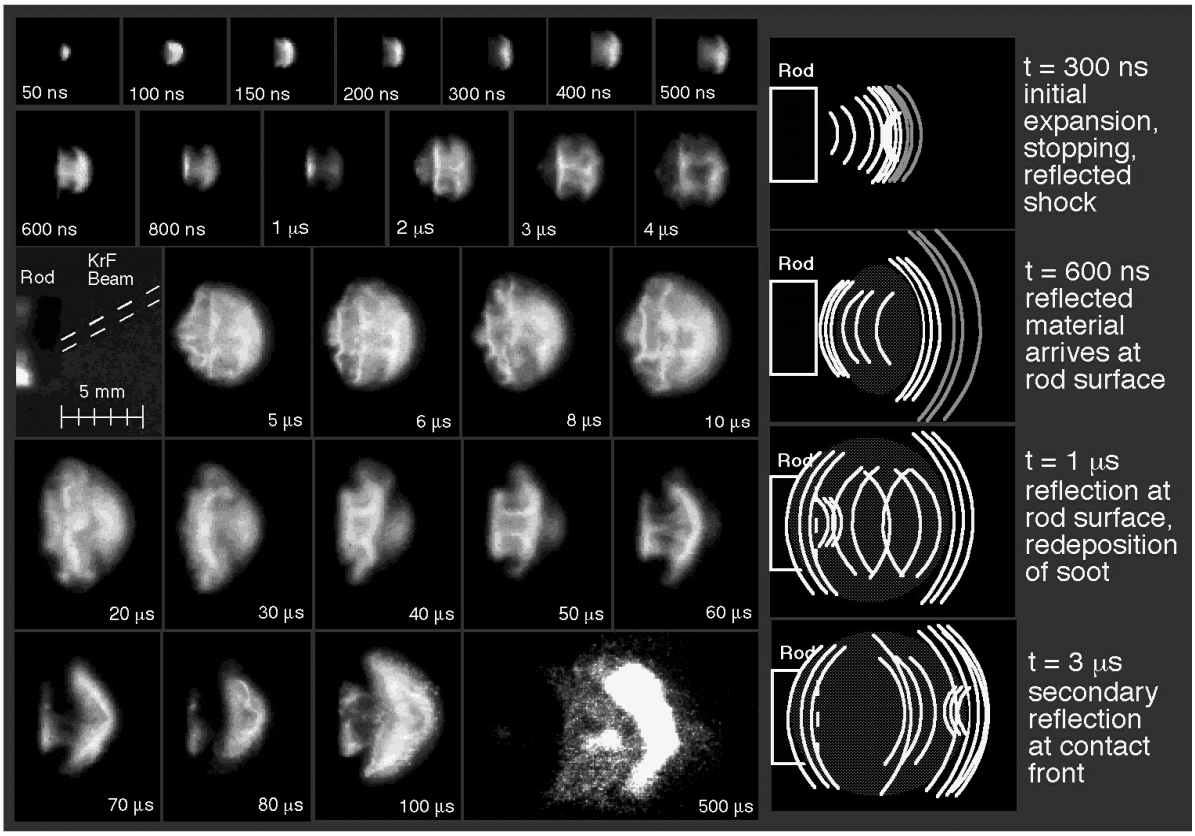

Fig. 4. Gated ICCD photographs of the visible plume luminescence following KrF-laser ablation (20 J cm^{-2}, 46ns FWHM pulse) of graphite into room-temperature 300 Torr Argon at the indicated time delays following laser arrival. When high laser pulse energies such as these are employed, several sets of reflected shocks are generated inside the plume (as diagrammed at right), leading to redeposition of small clusters as the plasma wraps back around the rod (see 5–30 μs images). The side-on view of the graphite rod, scale, and band of redeposited soot is shown in the inset (the rod surface in the 20–100 μs images is offset by 1.5 scale-mm further left). Several reflected shocks are evident. The first begins ~ 300 ns, resulting in backward-moving material leading to redeposition of soot on the rod sides, and another reflected shock from the rod surface (~1 μs). This process is repeated, the plume expanding in stages, until glowing microparticulates are observed away from the target at very long times (see 500 μs image). In these room-temperature experiments designed to generate fullerenes, Fourier transform mass spectrometry revealed no fullerenes in the soot redeposited back on the target (for $\Delta t < 30$ μs), but large quantities in the region corresponding to the glowing clusters and nanoparticles. See Ref. 28 for full details.

motion efficiently traps aggregated nanoparticles in a confined volume for long times (~ 3 s within ~1 cm^3 in this study) as shown in Fig. 5(a).

The leading edge of the plume in Fig. 6(a) propagates with velocities of: 10^3 cm/s between 200 μs $< \Delta t <$ 2 ms; 50 cm/s for 10ms $< \Delta t <$ 50 ms; and 6 cm/s during 30 ms $< \Delta t <$ 200 ms. After Δt = 2 s the plume stops moving upstream, and the plane of the vortex ring tilts toward the tube axis, possibly due to flow currents or thermophoretic forces. The plume is then dragged by the gas flow back to the collector with an estimated flow velocity of 0.6 cm/s. Finally, nanotubes and unconverted soot deposit on the cool collector surface by thermophoresis [25].

At room temperature the plume dynamics at later times are completely different. As shown in Fig. 6, the plume propagates slower in the axial direction. The motion of the material within the plume is highly turbulent. This turbulent behavior can be seen more explicitly using Rayleigh scattering from the nanoparticles which form during the cooling of the laser plasma in the background gas.

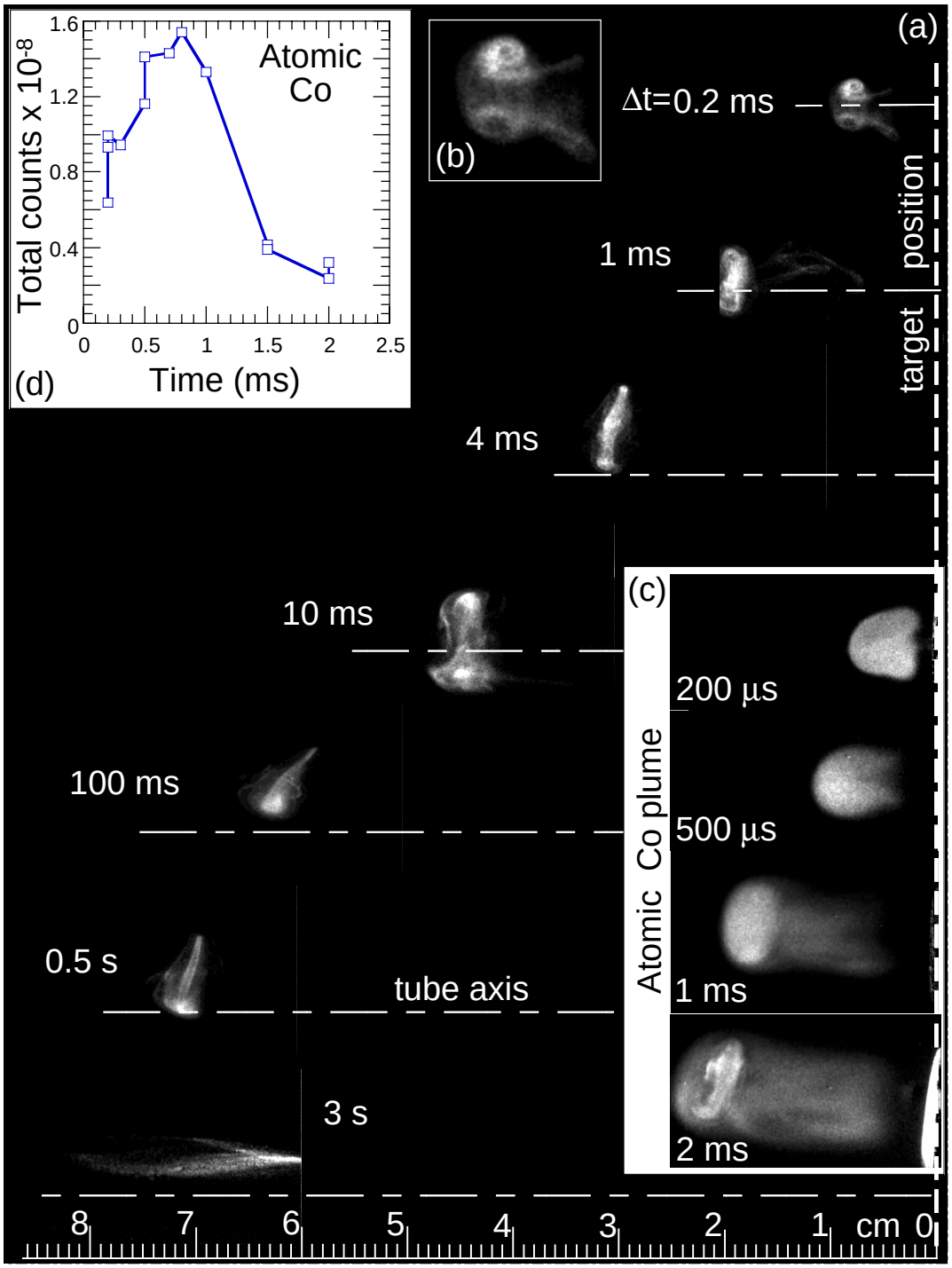

Fig. 5. Laser-induced luminescence (LIL) images of the C/Ni/Co plume during SWNT synthesis. A Nd:YAG-laser vaporizes a C/Co/Ni target (right edge of figure) inside a 2-in. quartz tube at 1000 ^{o}C in 500 Torr Ar (flowing to the right at 100 sccm). Each image represents a different ablation event. (a) Unfiltered images show the location of all C/Co/Ni species during nanotube growth (100 ns gate width, opened $\Delta\tau$ = 100 ns after the XeCl-laser pulse). (b) Maginified image at Δt = 0.2 ms, showing ring vortex hydrodynamic structure. (c) Selective imaging in the 320-380 nm spectral region to locate ground-state atomic Co in the plume (100 ns gate width, $\Delta\tau$ = 0). (d) Temporal history of the total number density of ground-state atomic Co, determined from integrating the LIL from a complete set of atomic-Co images shown in (b).

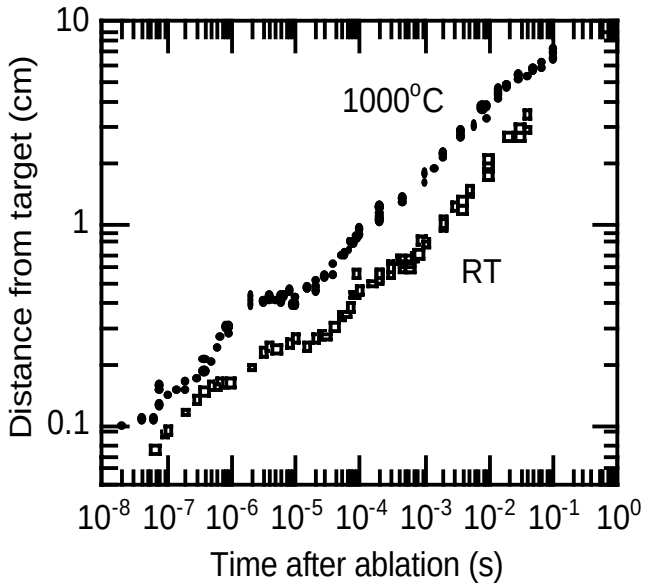

Fig. 6. Propagation of the leading edge of the ablation plumes at room temperature (RT) and at 1000°C.

Rayleigh-scattering images were obtained to track the plume evolution from a pure graphite target after KrF-laser ablation into room-temperature 300 Torr Ar, an example of which is given in Figure 7. By comparing images of the plasma with and without secondary laser-irradiation, the emergence of Rayleigh scattering was used to estimate the onset of plume condensation into nanoparticles [25]. Under these conditions, this time is estimated at 150 μs after ablation from these images. The highly turbulent behavior evident in the images likely results from the higher background gas density and smaller gas viscosity compared to those at 1000 °C. Despite the plume expansion, the ablated material remains confined to a relatively small volume within the thin sheets of multiple vortices.

Once the plume was located with ICCD-imaging, several spectroscopic techniques were applied to probe its composition, including: optical emission spectroscopy (OES) from excited states in the plasma; optical absorption spectroscopy (OAS) and laser-induced fluorescence (LIF) from ground-state atoms and molecules; laser-induced blackbody emission and Rayleigh scattering from clusters, nanoparticles, and nanotubes.

To understand the nature of the carbon species ejected from the target, OAS was performed in vacuum [32]. Low-resolution (2.6 nm) absorption spectra of the plume from a pure graphite target reveals a spectrum which is dominated by C_3 absorption via $A\ ^1\Pi_u \leftarrow X\ ^1\Sigma_g$ and C_2 absorption: in the Δv=-2, -1, 0, and +1 sequences of the Swan $d\ ^3\Pi_g \leftarrow a\ ^3\Pi_u$ system; and the $\Delta v = 0$ sequence of the Mulliken $D\ ^1\Sigma_u^+ \leftarrow X\ ^1\Sigma_g^+$ system.[27] The dominance of C_3 as the principal component of the plume is consistent with mass spectrometric measurements under the same conditions which show that the composition of the plume is primarily C_3, C_2, and C with very few higher-order clusters (intensity ratio, $C:C_2:C_3C_4:C_5$ = 56:35:100:2.5:1.6) [33].

Ground-state C_3 in the plume was probed by laser induced fluorescence with a 308-nm XeCl laser. Figure 8 shows the LIF spectrum of vaporized graphite in vacuum, displaying predominantly $C_3\ A\ ^1\Pi_u \rightarrow X\ ^1\Sigma_g$ emission (resolution 10 nm). In addition, weak Δv=0 C_2 Swan $d\ ^3\Pi_g \rightarrow a\ ^3\Pi_u$ emission can be observed at 516 nm. The XeCl laser can also excite vibronically-induced absorption of C_3 via $^1\Pi_\gamma$ and/or $^1\Delta_\upsilon \leftarrow X\ ^1\Sigma_\gamma$[34].

In addition, the XeCl laser can induce emission from atomic Co (via $a\ ^4F_J \leftarrow y\ ^4G^o_J$) and from atomic Ni (via $a\ ^3D_1 \leftarrow y\ ^3D^o_2$). It therefore serves as an excellent probe of the ground state atoms and molecules in the plume, both for laser-induced luminescence (LIL) spectroscopy, and spectroscopic imaging (see below) of the separate components.

From sets of images as in Fig. 5, both OES and LIL-spectra were acquired at 1000°C and at room temperature (RT). Figure 9 presents an abbreviated summary of these spectra, with the nascent plasma emission plotted along with the LIL-emission whenever

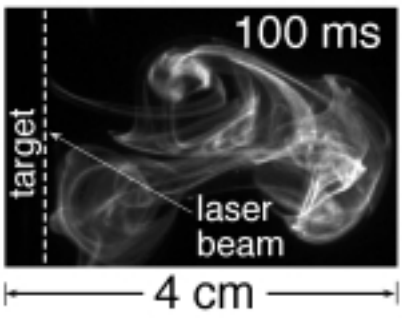

Fig. 7. Aggregated nanoparticles are confined to thin sheets at room temperature following laser ablation, as revealed by ICCD-imaging of Rayleigh-scattered light from a time-delayed 308-nm laser pulse. Graphite ablation into 300 Torr Ar.

both could be detected. The full sets of spectra are given in Ref. 27. At early times in the plume expansion, close to the target while the plasma is very hot, the plume species are primarily electronically excited and this emission from excited states dominates any laser-induced luminescence (from the ground-states) both at 1000 °C and at RT. Bright nascent emission from C_2 ($d\ ^3\Pi_g$ –> $a\ ^3\Pi_u$, Swan system) and C_3 ($A^1\Pi_u$–>$X^1\Sigma_g$) dominate at these times. As the plasma expands, cools, and recombines, the ground states become populated, and LIL-emission emerges to compete with the residual plasma emission. At 1000°C, LIL from atomic Co in the 320 – 380 nm range (see high-resolution spectrum inset in Fig. 9) is clearly visible. Finally, the nascent plasma emission completely disappears, and only LIL from ground-states remains. From previous measurements of clustering in laser plasmas expanding into background gases, this disappearance of the nascent plasma emission usually signals the onset of nanoparticle formation [23-25].

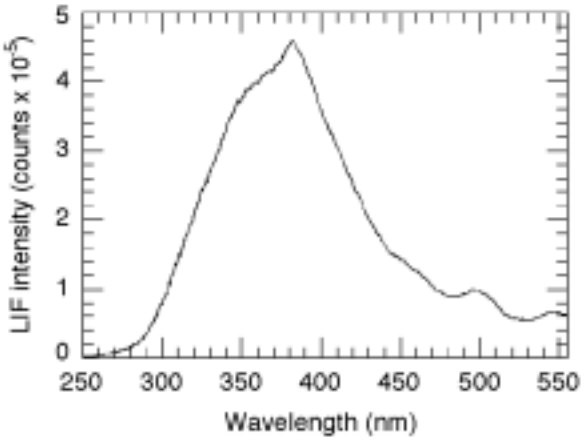

Fig. 8. LIF (XeCl-laser, 20 mJ/cm^2)- spectrum of C_3 in the carbon vapor plume generated by 248-nm ablation in vacuum.

Laser-induced blackbody radiation can be used to signal the presece of carbon clusters [35], nanoparticles [36], and nanotubes. The intensity of this blackbody emission, I, is defined by, A is a constant

$$I = Ar^3(T_0+\Delta T)^5 \qquad (1)$$

and r is the cluster radius.

Induced blackbody radiation becomes observable for $\Delta t > 200$ μs at 1000 °C (Fig. 9) and for $\Delta t > 50$ μs at room temperature, coincident with the disappearance of the C_2 and C_3 bands in both the plasma-emission and the laser-induced spectra for $\Delta t > 200$ μs at 1000 °C (and $\Delta t > 50$ μs at room temperature). From these two coincident measurements, we conclude that the carbon in the plume has all converted into clusters or larger aggregates by these times.

However, the atomic Co in the plume remains in atomic form long after the atomic and molecular carbon has disappeared. Integrating the emission in the 320–380 nm range from the LIL-spectra, the

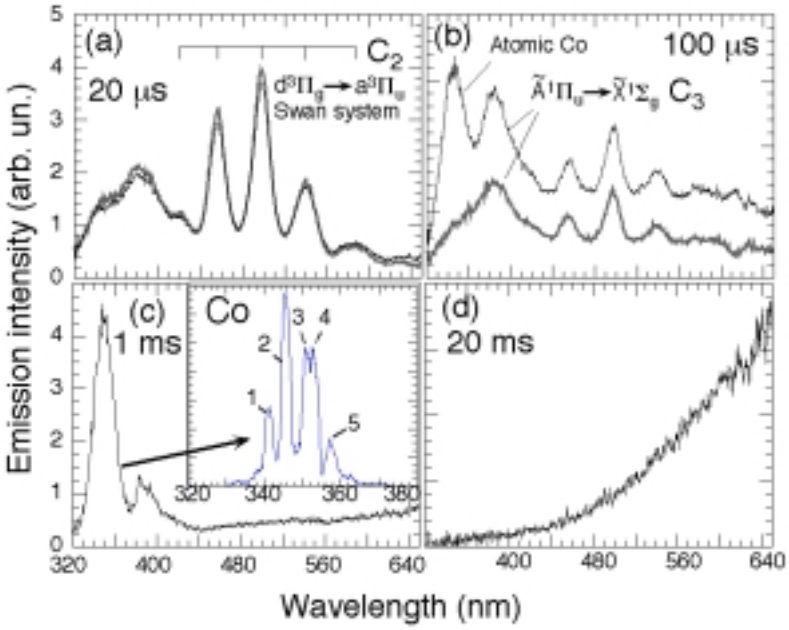

Fig. 9. Plasma emission (grayed) and laser-induced luminescence (dark) spectra measured at different time delays after the ablation laser pulse, Δt, and distances, x, from the target: (a) $\Delta t = 20$ μs, x = 0.2 cm (b) $\Delta t = 100$ μs, x = 0.5 cm (c) $\Delta t = 1$ ms, x = 2 cm and (d) $\Delta t = 20$ ms, x = 5 cm. Acquisition times of 100 ns [(a), (b)] and 3.5 μs [(c), (d)] began 50 ns after the XeCl-laser pulse. The inset in (c) shows a 1.3-nm resolution spectrum of induced fluorescence from the following transitions: (1) $b^4F_{7/2}$-$y^2G^o_{9/2}$ at 341.23 nm (2) $b^4F_{9/2}$-$y^4G^o_{11/2}$ at 345.35 nm (3) $b^4F_{5/2}$-$y^4G^o_{7/2}$ at 350.98 nm (4) $b^4F_{7/2}$-$y^4G^o_{9/2}$ at 352.98 nm, and (5) $b^4F_{5/2}$-$y^4D^o_{5/2}$ at 357.50 nm.

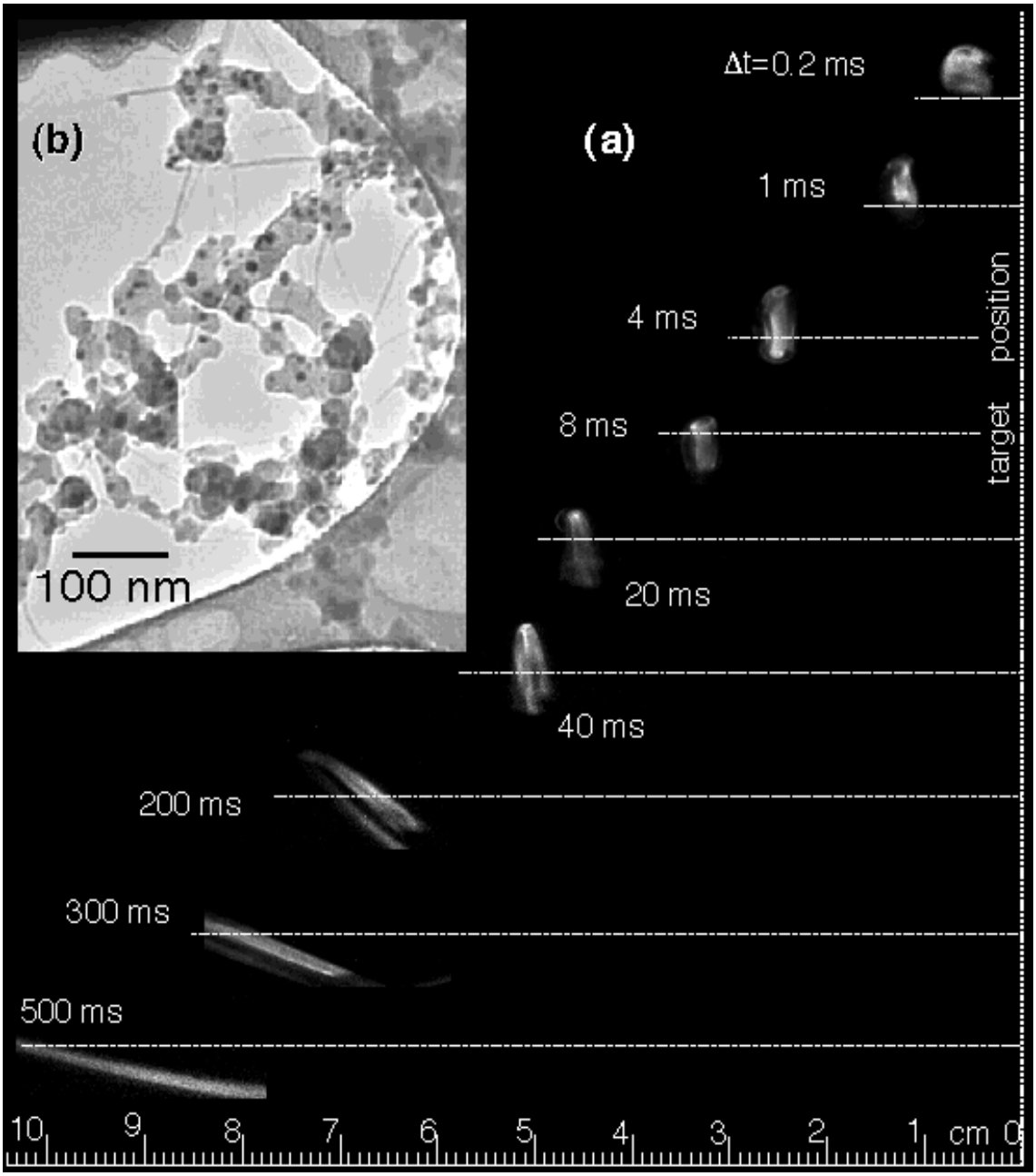

Fig. 10. (a) Laser-induced luminescence (LIL) images of the C/Ni/Co plume during synthesis of SWNT with controlled growth times of ~0.5 s. The target was positioned at d = 12.5 cm in Fig. 1. **(b)** Corresponding deposit collected at point 1 in Fig. 1, showing short (~100 nm) SWNT in the early stages of growth along with unconverted amorphous carbon particles and accompanying catalyst nanoparticles (dark dots) supported on holey carbon grid.

ground-state Co population is observed to peak at $\Delta t = 0.8$ ms and drop by an order of magnitude by $\Delta t = 2$ ms, permitting estimates of the Co clustering time of ~ 2 ms at 1000 ^{o}C (~ 1 ms at room temperature). A similar estimation for the Co clustering time was performed using spectroscopic imaging of the Co vapor plume [27].

Blackbody radiation remains the only feature of the spectra taken for $\Delta t > 2$ ms at 1000 ^{o}C. At room temperature the laser induced blackbody radiation disappears rapidly ($\Delta t \sim 5$ ms) for the

low XeCl-laser intensity employed here [chosen for use at T_0=1000°C in equation (1)]. The last recognizable feature of the spectrum is a broad band at 380 nm, which is currently unidentified.[27]

Hot particulates from the target would be easily imaged via their blackbody emission [37] or by Rayleigh-scattering. It is important to note that we observed very few particulate ejecta for the properly outgassed, hard, Dylon-fabricated targets used in this study.

Once sharp spectral features have been identified throughout a set of spectroscopic data (such as those described in section 4), optical filters can be used in conjunction with ICCD-imaging to selectively image different constituents of the plume. In Figure 5(c), the 320–380 nm spectral region was imaged at 1000°C to selectively image the ground-state atomic Co in the plume. Similar images of the plume from a pure carbon target revealed negligible contribution to the overall intensity in this spectral region from carbon species' blackbody emission.[27]

The total integrated emission from these images gives the time dependence of the atomic Co in the plume. Shown in Figure 5(d), the ground-state atomic Co population is observed to rise (due to population of the ground states via recombination of the hot plasma) and then decay as these atoms become incorporated in clusters. This time dependence confirmed the spectral measurements summarized in Figure 9.

The relatively uniform distribution of the atomic Co in the plume observed with spectroscopic imaging contrasts with the vorticity of the clustered carbon species emitting blackbody radiation (compare 1-ms images in Figs. 5(a) and 5(c); a more detailed comparison is given in Ref. 27). This provides further evidence of the sequential condensation of carbon and cobalt into clusters. We believe that the higher diffusivity of the atomic Co effectively competes with the hydrodynamic trapping within the vortex during this time. During the condensation of the Co atoms for $\Delta t > 1$ ms, only the leading edge of the atomic-Co plume overlaps the carbon clusters. Assuming that Co clustering initiates nanotube formation, it appears that nanotubes grow from a feedstock of aggregated nanoparticles during seconds of time, confined first within the vortex ring and then by thermophoresis and fluid flow in the quartz tube.

In order to check this conclusion and estimate the growth rate, the target was positioned closer to the front furnace edge (d = 12.5 cm in Fig. 1) such that the plume spent only ~ 0.5 s within the hot zone before exiting the furnace in the upstream direction (as shown in Fig. 10(a)). From estimates of heat transfer coefficients and the thermal diffusivity of the gas (convection currents were not considered) the thermal gradient near the upstream edge of the furnace was estimated to extend ~ 5 cm into the tube (d > 7 cm in Fig. 10(a)). Thermophoresis is a powerful driving force for gas-suspended nanoparticles, driving them toward cooler regions of the growth chamber (and permitting capture of the nanomaterials on the collector) [25]. The intention in this experiment was to utilize the natural plume velocity in the upstream direction (determined from Fig. 6) to drive the plume into the region of the thermal gradient near the upstream edge of the furnace. LIL-ICCD imaging recorded the plume dynamics from ablation to deposition.

The plume motion in Fig. 10(a) is quite similar to that of Fig. 5 for $\Delta t < 100$ ms. However, for $\Delta t > 100$ ms the plume propagation changes dramatically, i.e. the plane of the ring vortex tilts relative to the tube axis and the ring elongates along this axis. Between 0.5–0.7 s the plume exits the furnace in this tilted orientation to deposit onto the upper surface of the quartz tube (at point 1 in Fig. 1).

A transmission electron microscopy (TEM) image of this deposit is shown in Fig. 10(b). The collected material consists of aggregated carbon and metal-catalyst nanoparticles, and thin SWNT bundles of only ~ 100 nm length. The relative yield of the carbon particles is larger than the yield of the carbon nanotubes which clearly shows that the time spent by the plume in the hot zone (~ 0.5 s) was not sufficient to convert all of the carbon material into nanotubes. This combined imaging and TEM analysis permits the average growth rate at 1000 °C to be estimated at ~ 0.2 μm/s.

CONCLUSIONS

In summary, we have used laser-induced imaging and spectroscopy diagnostic techniques, along with ex situ TEM, to determine that single-walled carbon nanotubes form over several seconds inside the hot furnace after laser vaporization. Size-controlled SWNT were formed in short 100-nm lengths by controlling the growth time with these diagnostics to ~ 0.5 s, yielding

0.2 μm/s for the first estimate of the SWNT growth rate by LV. The spectroscopy at early times after laser ablation indicates that the plume initially consists of atomic and molecular species, with no evidence of hot molten particulates which were recently suggested as the primary ejecta [38]. Condensation of carbon occurs within 0.2 ms after ablation, while atomic Co condenses much later (between 1.5 and 2 ms) at 1000 ^{o}C. From our time-resolved growth experiments, we conclude that the great majority of single-wall carbon nanotube growth occurs during very long periods of time (several seconds) within the vortex ring which serves to hydrodynamically trap the gas-suspended clusters and aggregates within a ~1 cm^3 volume. Assuming that metal catalyst clusters are required before carbon nanotube growth begins, we conclude that the feedstock for nanotube growth during this annealing time within the oven is this mixture of carbon and metal catalyst nanoparticles. As we demonstrated, this provides an opportunity for the growth of controlled lengths of SWNT by controlling the annealing time spent inside the oven. The mechanism for SWNT growth clearly appears to involve the condensed phase conversion of amorphous carbon nanoparticles by molten metal-catalyst alloy nanoparticles. It is quite possible that the carbon clusters serve as the condensation centers for the metal clusters, and mixed carbon-catalyst alloy clusters are produced. In support of the condensed phase conversion growth mechanism, preliminary experiments have shown that *ex situ* annealing of the mixture of short SWNT "seeds" and nanoparticles examined in Fig. 10(b) resulted in continued growth of SWNT bundles of greatly increased lengths and increased diameters, similar to those produced by annealing within the oven just after laser-vaporization and condensation (as shown in Figure 5). Finally, we produced high-purity SWNT deposits with laser repetition rates as low as 0.016 Hz, where *in situ* imaging directly confirmed that each plume left the oven before the next laser pulse. Through these images of the growth process, we conclude that long (~10 μm) SWNT can form from the small amount of material vaporized in a single-laser shot, a remarkable feat of self-assembly.

ACKNOWLEDGMENTS

The authors gratefully acknowledge research discussions with D. J. Rader and the expert assistance of S. Lowe with this manuscript. This work was sponsored by the Division of Material Science, U. S. Department of Energy under Contract No. DE-AC05-96-R22464 with Lockheed Martin Energy Research Corp. and by the Laboratory-Directed Research and Development Program at ORNL.

REFERENCES

1. A. Thess, R. Lee, P. Nikolaev, H. Dai, P. Petit, J. Robert, C. Xu, Y. H. Lee, S. G. Kim, A. G. Rinzler, D. T. Colbert, G. E. Scuseria, D. Tomanek, J. E. Fisher, R. E. Smalley, *Science* 273, 483 (1996).
2. M. Yudasaka, T. Ichihashi, T. Komatsu, S. Iijima, *Chem. Phys. Lett.* 299, 91 (1999).
3. A. G. Rinzler, J. Liu, H. Dai, P. Nikolaev, C. B. Huffman, F. J. Rodriguez-Macias, P. J. Boul, A. H. Lu, D. Heymann, D. T. Colbert, R. S. Lee, J. E. Fisher, A. M. Rao, P. C. Eklund, R. E. Smalley, *Appl. Phys. A* 67, 29 (1998).
4. Hu JT, Odom TW, Lieber CM, *Accounts of Chemical Research* 32, 435-445 (1999).
5. A. C. Dillon, P. A. Parilla, K. M. Jones, G. Riker, M. J. Heben, *Mater. Res. Symp. Proc*. (to be published).
6. F. Kokai, K. Takahashi, M. Yudasaka, R. Yamada, T. Ichihashi, and S. Iijima, *J. Phys. Chem.* B 103, 4346 (1999).
7. B.I. Yakobson and R.E. Smalley, *American Scientist* 85, 324 (1997).
8. S. Iijima, T. Ichihashi, *Nature* 363, 603 (1993).
9. D.S. Bethune, C.H. Kiang, M.S. de Vries, G. Gorman, R. Savoy, J. Vazquez, R. Beyers, *Nature* 363, 605 (1993).
10. Ph. Avouris, T. Hertel, R. Martel, T. Schmidt, H.R. Shea, and R.E. Walkup, *Appl. Surf. Sci.* 141, 201 (1999).

11. R.H. Baughman, C. Cui, A.A. Zakhidov, Z. Iqbal, J. N. Barisci, G. M. Spinks, G. G. Wallace, A. Mazzoldi, D. De Rossi, A. G. Rinzler, O. Jaschinski, S. Roth, and M. Kertesz, *Science* 284, 1340 (1999).
12. P. Poncharal, Z. L. Wang, D. Ugarte, and W. A. de Heer, *Science* 283, 1513 (1999).
13. S.S. Wong, E. Joselevich, A.T. Woolley, C.L. Cheung, and C.M. Lieber, *Nature* 394, 52 (1998).
14. H. Schmid and H.–W. Fink, *Appl. Phys. Lett.* 70, 2679 (1997).
15. J. Li, C. Papadopoulos, J. M. Xu, and M. Moskovits, *Appl. Phys. Lett.* 75, 367 (1999).
16. J. Liu, A. G. Rinzler, H. Dai, J. H. Hafner, R. K. Bradley, P. J. Boul, A. Lu, T. Iverson, K. Shelimov, C. B. Huffman, F. Rodriguez–Macias, Y.–S. Shon, T. R. Lee, D. T. Colbert, and R. E. Smalley, *Science* 280, 1253 (1998).
17. Y. Ye, C. C. Ahn, C. Witham, B. Fultz, J. Lku, A. G. Rinzler, D. Colbert, K. A. Smith, and R. E. Smalley, *Appl. Phys. Lett.* 74, 2307 (1999).
18. T. Guo, P. Nikolaev, A. Thess, D. T. Colbert, R. E. Smalley, *Chem. Phys. Lett.* 236, 419 (1995).
19. C. Journet, W. K. Maser, P. Bernier, A. Loiseau, M. Lamy de la Chapelle, S. Lefrant, P. Deniard, R. Lee, J.E. Fisher, *Nature* 388, 756 (1997).
20. H. M. Cheng, F. Li, G. Su, H. Y. Pan, L. L. He, X. Sun, M. S. Dresselhaus, *Appl. Phys. Lett.* 72, 3282 (1998).
21. B. C. Satiskumar, A. Govindaraj, R. Sen, C.N.R. Rao, *Chem. Phys. Lett.* 293, 47 (1998).
22. S. Arepalli, C.D. Scott, *Chem. Phys. Lett.* 302, 139 (1999).
23. D.B. Geohegan, A.A. Puretzky, G. Duscher and S.J. Pennycook, *Appl. Phys. Lett.* 72, 2987 (1998).
24. D.B. Geohegan, A.A. Puretzky, G. Duscher and S.J. Pennycook, *Appl. Phys. Lett.* 73, 438 (1998).
25. D.B. Geohegan, A.A. Puretzky, D.J. Rader, *Appl. Phys. Lett.* 74, 3788 (1999).
26. A. A. Puretzky, D. B. Geohegan, X. Fan, and S. J. Pennycook, *Appl. Phys. Lett.* **76**, 182 (2000).
27. A. A. Puretzky, D. B. Geohegan, X. Fan, and S. J. Pennycook, special issue of *Appl. Phys.A.*to be published Jan./Feb. 2000.
28. David B. Geohegan, A. A. Puretzky, R. L. Hettich, X.-Y. Zheng, R. E. Haufler, and R. N. Compton, in *Advanced Materials '93, IV/ Laser and Ion Beam Modification of Materials*, edited by I. Yamada, et al., Trans. Mat. Res. Soc. Jpn., 17, 349 (1994).
29. Images also available online at www.ornl.gov/~odg.
30. A. V. Bulgakov and N. M. Bulgakova, *J. Phys. D: Appl. Phys.* 31, 693 (1998).
31. F. Garrelie, C. Champeaux, A. Catherinot, *Appl. Phys. A* 69, 45 (1999).
32. D. B. Geohegan, A. A. Puretzky, *Appl. Phys. Lett.* 67, 197 (1995).
33. D. Krajnovich, *J. Chem. Phys* 102, 726 (1995).
34. E. A. Rohlfing, *J. Chem. Phys* 91, 4531 (1989).
35. D. B. Geohegan, A. A. Puretzky, *Mater. Res. Symp. Proc*. 397, 55 (1996).
36. E. A. Rohlfing, *J. Chem. Phys.* 89, 6103 (1988).
37. D. B. Geohegan, *Appl. Phys. Lett*. 62, 1463 (1993).
38. M. Yudasaka, R. Yamada, N. Sensui, T. Wilkins, T. Ichihashi, and S. Iijima, *J.Phys. Chem.* B 103, 6224 (1999).